Chinese Chemical Letters 34 (2023) 107840

Contents lists available at ScienceDirect

Chinese Chemical Letters

journal homepage: www.elsevier.com/locate/cclet

Free-standing $SnNb_2O_6$@CSN film as flexible anode for high performance sodium-ion batteries

Xuemin Yin[a], Tao Liu[a], Xiuping Yin[a], Xiaochen Feng[a], Yiming Liu[a], Qinhao Shi[a], Xingli Zou[b], Yufeng Zhao[a,*]

[a] *Institute for Sustainable Energy and College of Sciences, Shanghai University, Shanghai 200444, China*
[b] *Department of Materials Science and Engineering, Shanghai University, Shanghai 200072, China*

ARTICLE INFO

Article history:
Received 5 August 2022
Revised 13 September 2022
Accepted 20 September 2022
Available online 11 May 2023

Keywords:
Free-standing
$SnNb_2O_6$@CSN
Anode
Sodium-ion batteries
Flexible material

ABSTRACT

Free-standing electrodes are promising candidates for flexible rechargeable batteries, toward the application of flexible energy storage devices, due to their merits of additive-free, lightweight, and high energy density. Herein, we report a free-standing $SnNb_2O_6$@CSN flexible film with $SnNb_2O_6$ encapsulated in 3D carbon skeleton nanofibers by electrospinning and carbonization processes as flexible anode for sodium-ion batteries (SIBs). The 3D carbon skeleton nanofibers serve as ion/electron transport pathway to improve the electrochemical reaction kinetics and meanwhile alleviate the volume changes of $SnNb_2O_6$ during charge-discharge processes. The as-constructed half-cell ($SnNb_2O_6$@CSN‖Na) exhibits excellent cycling stability of 99.2 mAh/g at 0.5 A/g after 950 cycles (coulombic efficiency of ~100%) and a high rate performance of 108.6 mAh/g at 10 A/g. In addition, the pouch cell can light up the LEDs at different bending angles (0°, 90°, 180°). This research shows a promising anode material for flexible energy storage electronics.

In recent years, environmental pollution and fossil energy crisis have triggered the rapid development of cost-effective energy storage devices. Sodium-ion batteries (SIBs) are considered as promising candidates to lithium-ion batteries (LIBs) due to their low cost and abundant resources [1–6]. Nevertheless, due to the ion radius of Na^+ (1.02 Å) is larger than that of Li^+ (0.76 Å), the electrode materials of SIBs exhibit sluggish kinetics and large volume changes during Na^+ intercalation/deintercalation processes [7–10].

To date, the reported anode materials for SIBs include carbon-based materials [11,12], alloys [8,13], titanium-based materials [14–16] and organic materials [17]. Among them, niobium-based layered oxides (*e.g.*, $TiNb_2O_7$, $CuNb_2O_6$, $BiNbO_4$, $SnNb_2O_6$, $ZnNb_2O_6$ and $SbNbO_4$) are considered as the promising anode materials due to the high theoretical capacity and excellent safety [18–21]. In particular, $SnNb_2O_6$ with forsterite structure has been widely used in the field of photocatalytic degradation due to its suitable energy band structure, special crystal structure and excellent chemical stability. In addition, $SnNb_2O_6$ is a typical layered oxide with large interlayer spacing, which can provide abundant channels for the transport of Na ions, so it is expected to be applied in Na-ion batteries [22,23]. For instance, we have previously fabricated $SnNb_2O_6$@C materials with carbon coating, which displays an outstanding electrochemical performance (67 mAh/g@10 A/g, 102.6 mAh/g@0.5 mA/g after 800 cycles) in SIBs [24]. Huang and co-workers [21] prepared $SnNb_2O_6$/amino-functionalized graphene composite by self-assembly method as anode material for SIBs, which presents a high rate performance of 118 mAh/g at 0.8 A/g and excellent cyclability of 106 mAh/g at 0.5 A/g after 1900 cycles.

However, these electrodes were prepared by slurry coating method, in which binders, conductive agents and active materials were dissolved in organic solvent and then coated on copper current collector. The preparation process is complicated, and the active materials are easily detached from the current collector after multiple folds. To solve above issues, additive- and binder-free flexible electrodes were designed. Flexible electrode is a free-standing film that integrates current collector and active materials, which is not only easy to prepare, but also can be used in flexible electronic energy storage devices. Many flexible substrates, such as graphene [25], carbon cloth [26–28], carbon nanofibers/nanotubes and so forth [7,29–34], have been investigated for flexible electrodes. For example, we have previously reported a free-standing FeP@NPC electrode with FeP nanoparticles wrapped in nanofibers for flexible anode, which can be stable working under different folding conditions [29]. Liang and co-workers [35] prepared a self-supporting composite with $NiSe_2$ encapsulated in nanotubes as anode mate-

---

[*] Corresponding author.
E-mail address: yufengzhao@shu.edu.cn (Y. Zhao).

https://doi.org/10.1016/j.cclet.2022.107840
1001-8417/

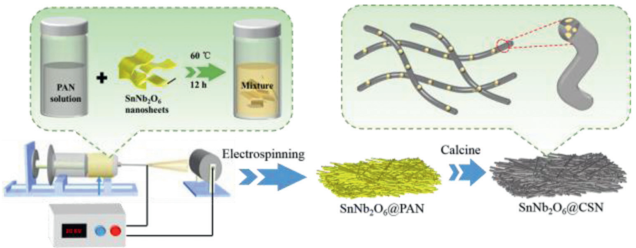

Fig. 1. The schematic illustration of the synthesis for free-standing $SnNb_2O_6$@CSN film.

rial, which displays significantly improved electrochemical performance. Some studies have reported that free-standing electrodes can effectively improve the electrochemical performance of batteries, but there are still some problems in the practical application of flexible energy storage devices. Therefore, designing and developing more kinds of flexible electrodes can provide more candidates for the development of flexible electronic devices. As a promising anode material, $SnNb_2O_6$ has not been reported as a flexible electrode for SIBs.

Herein, we report a free-standing 3D carbon skeleton nanofiber-encapsulated $SnNb_2O_6$ ($SnNb_2O_6$@CSN) film as anode material for SIBs by facile electrospinning and carbonization processes. The 3D carbon skeleton can not only shorten the transmission paths of electron/ion, improve the electrochemical reaction kinetics, but also prevent the active material from falling off the current collector during the charge and discharge processes. As expected, the as-synthesized free-standing $SnNb_2O_6$@CSN electrode exhibits high rate performance of 108.6 mAh/g at 10 A/g, and the pouch cell can still light up the LEDs after being folded several times, displaying that it is a promising anode material for flexible electronic devices.

As shown in Fig. 1 and Fig. S1 (Supporting information), the $SnNb_2O_6$@CSN film was prepared *via* multi-steps including solvothermal process, electrostatic spinning, and high temperature carbonization (Fig. S2 in Supporting information). Firstly, $SnNb_2O_6$ material was synthesized by a classical solvothermal method, and its color is yellow (Fig. S3a in Supporting information). The morphology of $SnNb_2O_6$ presents irregular lamellar structure, the average thickness of $SnNb_2O_6$ nanosheet is about 40 nm (Figs. 2a and b, Fig. S4 in Supporting information). Subsequently, the $SnNb_2O_6$ nanosheets were dissolved in polyacrylonitrile (PAN) solution to obtain $SnNb_2O_6$@PAN nanofiber film by electrospinning (Fig. S3b in Supporting information). Finally, $SnNb_2O_6$@PAN film was calcined at 700 °C in argon atmosphere to obtain the final products ($SnNb_2O_6$@CSN). As shown in Fig. 2c, the diameter of $SnNb_2O_6$@CSN nanofiber is 300–400 nm, and the $SnNb_2O_6$ were encapsulated inside carbon nanofibers. The optical images of $SnNb_2O_6$@CSN film in Fig. 2d exhibit the excellent flexibility at different states, indicating that the obtained $SnNb_2O_6$@CSN film possesses good self-supporting flexibility.

The microstructures of the resulting materials were characterized in detail. Figs. 2e and f show the TEM and HRTEM images of the $SnNb_2O_6$. It can be seen that there are distinct fringes with lattice spacing of about 0.36 nm, corresponding to the $(\bar{1}11)$ lattice plane of $SnNb_2O_6$ [36]. Figs. 2g–i illustrate the TEM and HRTEM images of the $SnNb_2O_6$@CSN nanofiber, and it can be clearly seen that the $SnNb_2O_6$ were encapsulated in nanofibers. Moreover, the lattice fringe of $SnNb_2O_6$@CSN sample can be observed in Fig. 2i, which is consistent with the structure of $SnNb_2O_6$ nanosheet. Energy dispersive spectroscopy (EDS) mapping test was shown in Figs. 2j–o, it can be seen that carbon, oxygen, niobium and stannum are distributed in the nanofiber, manifesting that the $SnNb_2O_6$ nanosheets were encapsulated in the nanofiber.

As displayed in Fig. 3a, the XRD pattern shows that all diffraction peaks of $SnNb_2O_6$ are good matched with the foordite structured $SnNb_2O_6$ (with a typical layered structure, JCPDS No. 84-1810) and no other impure signals are detected, indicating the $SnNb_2O_6$ has high crystallinity. Nevertheless, the diffraction peaks of $SnNb_2O_6$@CSN are relatively weak, which is attributed to the carbon coating. In addition, the surface elemental composition and elemental valence states of $SnNb_2O_6$@CSN were characterized by XPS. The survey spectrum of $SnNb_2O_6$@CSN film (Fig. 3b) displays characteristic peaks of carbon, oxygen, niobium and stannum, indicating that there is no impurity in $SnNb_2O_6$@CSN. Notably, the peak intensity of C 1s is significantly stronger than that of other elements, indicating a higher carbon content in $SnNb_2O_6$@CSN film. Fig. 3c shows that the Sn 3d XPS spectrum was split into two peaks at 495.3 and 486.7 eV, which could be assigned to the Sn $3d_{3/2}$ and Sn $3d_{5/2}$ of $SnNb_2O_6$, respectively [36,37]. The Nb 3d XPS spectrum in Fig. 3d presents two characteristic peaks located at 209.9 and 207.2 eV, which can be attributed to the spin-orbit peaks of Nb $3d_{3/2}$ and Nb $3d_{5/2}$, respectively, indicating that the chemical valence state is Nb^{5+} [23,38]. The O 1s spectrum displays three peaks at 530.6, 531.8, and 533.5 eV, corresponding to the Nb-O/Sn-O, C-O, and C=O bonds, respectively (Fig. 3e) [39]. Fig. 3f shows that the C 1s spectrum at 284.8, 285.9, and 289.9 eV can be ascribed to the C-C, C-O and C=O bonds, respectively, which is consistent with the O 1s results [40]. The XPS spectra of the $SnNb_2O_6$ nanosheets are shown in Fig. S5 (Supporting information). In addition, the $SnNb_2O_6$ content in $SnNb_2O_6$@CSN (~44.7 wt%) was calculated by thermogravimetric analysis (TGA) in Fig. S6 (Supporting information).

The electrochemical performance of free-standing $SnNb_2O_6$@CSN electrode for sodium-ion storage behavior was investigated, half-cell was assembled using sodium metal as the counter electrode (Fig. 4a). The cyclic voltammetry (CV) tests were performed in a range of 0.01–3.00 V at 0.1 mV/s. Fig. S7a (Supporting information) shows the first three CV profiles of the $SnNb_2O_6$@CSN electrode, the reduction peaks at 0.22 V and 0.40 V in the first discharge cycle should be attributed to the decomposition of $SnNb_2O_6$ to Sn and Nb_2O_6 and the establishment of the solid electrolyte interface (SEI), respectively [41,42]. The two cathodic peaks located at 0.24 and 0.78 V correspond to the dealloying process of Na_xSn [42]. The peaks at 1.29 V and 1.54 V are attributed to the extraction/insertion of Na^+ in the Nb_2O_5 [43]. It is worth noting that the following CV profiles are almost coincided, demonstrating the excellent electrochemical reversibility of the $SnNb_2O_6$@CSN electrode. The CV profiles of $SnNb_2O_6$ electrode were shown in Fig. S7b (Supporting information), it is clear that some peaks are present in the CV profiles of $SnNb_2O_6$ but not in the CV profiles of $SnNb_2O_6$ @CSN. For example, a pair of peaks around 0.05–0.1 V are in good agreement with redox peaks of super P [21,44]. In addition, it can be seen that there are two weak oxidation peaks around 2.1 V and 2.4 V in the CV profiles of $SnNb_2O_{6,}$ which should be attributed to the reaction between sodium ion and Cu_2O and CuO thin layer on the surface of the copper current collector [45,46].

The electrochemical performance of the free-standing $SnNb_2O_6$@CSN electrode was investigated. The discharge-charge profiles of $SnNb_2O_6$@CSN at the voltage range from 0.01 V to 3.00 V (*vs.* Na/Na^+) under a current density of 0.05 A/g are shown in Fig. S7c (Supporting information). The $SnNb_2O_6$@CSN electrode displays discharge and charge capacities of 570.0 and 339.1 mAh/g, respectively, with a coulombic efficiency (CE) of 59.5% in the initial cycle. A good electrochemical reversibility was achieved in the following charge-discharge cycles. However, the $SnNb_2O_6$ delivers discharge and charge capacities of 520.0 and 291.1 mAh/g, respectively, with a CE of only 56.0% in the initial cycle (Fig. S7d in Supporting information). The irreversible capacity loss could be

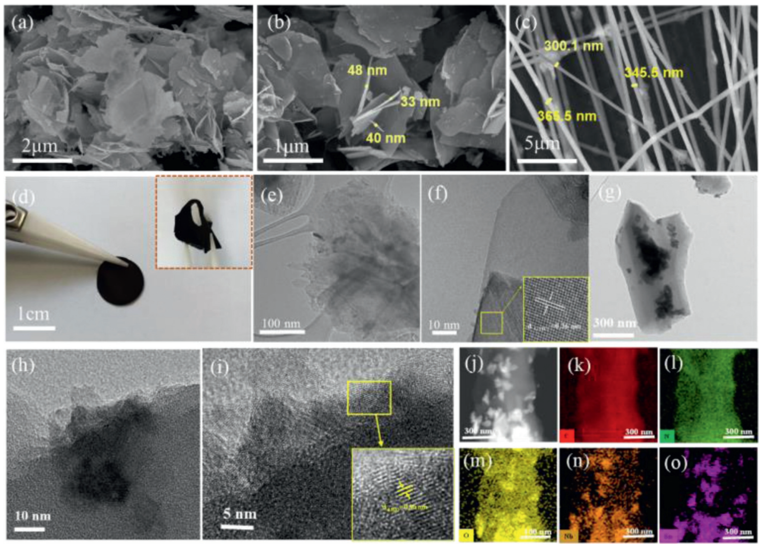

Fig. 2. (a, b) SEM images of the $SnNb_2O_6$ nanosheets. (c) SEM image of the $SnNb_2O_6$@CSN film. (d) Optical photographs of the $SnNb_2O_6$@CSN film at different states. The TEM and HRTEM images of (e, f) $SnNb_2O_6$ nanosheets and (g–i) $SnNb_2O_6$@CSN film. (j–o) Elemental mapping of C, O, N, Sn and Nb for $SnNb_2O_6$@CSN film.

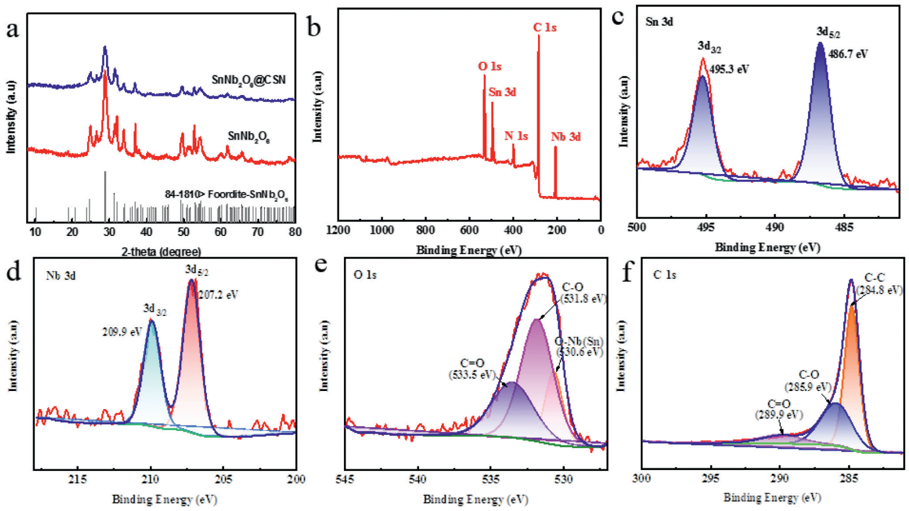

Fig. 3. (a) XRD patterns of the as-prepared $SnNb_2O_6$@CSN film and $SnNb_2O_6$. The XPS spectra of (b) full survey, (c) Sn 3d, (d) Nb 3d, (e) O 1s and (f) C 1s.

ascribed to the formation of solid electrolyte interface (SEI) and the irreversible reduction of $SnNb_2O_6$.

To investigated the cycling stability of $SnNb_2O_6$@CSN electrode and $SnNb_2O_6$ electrode, the cycle testing was carried out at a current density of 0.05 A/g. As shown in Fig. 4b, both materials exhibit large capacity loss in the first 30 cycles, which may be related to the formation of solid electrolyte interface (SEI), the volume change of the electrode material and the irreversible reduction of the $SnNb_2O_6$ during charging and discharging [47]. The reversible capacity of $SnNb_2O_6$@CSN electrode maintains at 175.1 mA/g after 240 cycles. While the reversible capacity of $SnNb_2O_6$ is only 111.1 mAh/g after 240 cycles. Significantly, the cycling stability of $SnNb_2O_6$@CSN electrode is superior to that of $SnNb_2O_6$. The long-term cycling stability of $SnNb_2O_6$@CSN was tested at a high current density of 0.5 mA/g. As shown in Fig. 4c, the reversible specific capacity is 99.2 mAh/g with a CE of ~100% after 950 cycles, indicating excellent cycling stability of the $SnNb_2O_6$@CSN electrode. In addition, the corresponding charge-discharge profiles of $SnNb_2O_6$@CSN at the 5th, 20th, 100th, 200th and 500th cycles are shown in Fig. S8a (Supporting information). While for $SnNb_2O_6$ electrode, the reversible specific capacity remains at 62.1 mAh/g after 950 cycles (Fig. 4c and Fig. S8c in Supporting information). The rate performance and cycling stability of the pure carbon nanofibers are shown in Fig. S9 (Supporting information). Furthermore, the $SnNb_2O_6$ electrode material was obviously detached from the copper current collector after 50 cycles (Fig. S10 in Supporting information). The cross-sectional thickness changes of $SnNb_2O_6$ and $SnNb_2O_6$@CSN electrodes were calculated in Fig. S11 (Supporting information). It can be seen that the expansion rate for the $SnNb_2O_6$ is 36.1%. while the thickness of the $SnNb_2O_6$@CSN electrode after 50 cycles is smaller than that of the initial electrode, which is mainly because the initial $SnNb_2O_6$@CSN film is relatively fluffy, the $SnNb_2O_6$@CSN film becomes thinner under certain pressure during cell assembly. In addition, the $SnNb_2O_6$@CSN electrode is loose and porous (Fig. 2c), which provides a certain space for the volume change of $SnNb_2O_6$ during charge-discharge processes.

The rate performances of the $SnNb_2O_6$@CSN and $SnNb_2O_6$ materials at various current densities were displayed in Fig. 4d. The $SnNb_2O_6$@CSN demonstrates the reversible specific capacities of 335.5, 283.9, 265.6, 234.7, 207.4, 174.3, 127.7 and 108.6 mAh/g at current densities of 0.05, 0.1, 0.2, 0.5, 1, 2, 5 and 10 A/g, re-

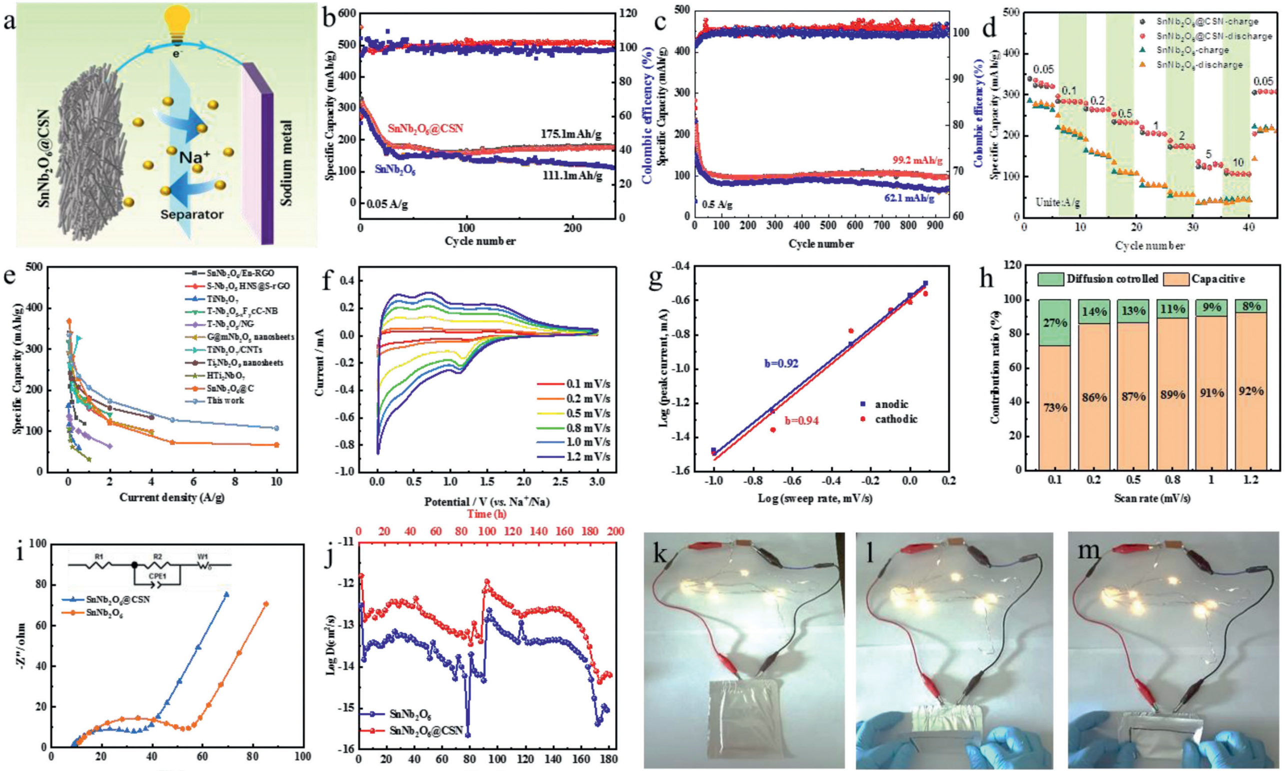

Fig. 4. (a) The schematic illustration of the $SnNb_2O_6$@CSN||Na half-cell. (b) Cycling stability of $SnNb_2O_6$ and $SnNb_2O_6$@CSN at 0.05 A/g. (c) Long-term cycling stability of $SnNb_2O_6$@CSN at 0.5 A/g. (d) Rate performances of the obtained materials at different current densities from 0.05 A/g to 10 A/g. (e) Comparison between $SnNb_2O_6$@CSN and other reported niobium-based composites. (f) CV curves of $SnNb_2O_6$@CSN at different scan rates. (g) log*i* *vs.* logυ plots of anodic/cathodic peaks for $SnNb_2O_6$@CSN. (h) Contribution rate of the capacitive and diffusion controlled of the free-standing $SnNb_2O_6$@CSN under different scan rates. (i) Nyquist plots of the as-prepared materials. (j) Na^+ diffusion coefficients for free-standing $SnNb_2O_6$@CSN and $SnNb_2O_6$. (k–m) the digital photos of pouch cell lighting up LED at different bending angles.

spectively. In addition, when the current density was returned to 0.05 A/g, the specific capacity of the $SnNb_2O_6$@CSN was restored to 308.3 mAh/g. In comparison, the $SnNb_2O_6$ exhibits the reversible specific capacities of 277.8, 218.8, 159.8, 113.3, 81.1, 56.7, 36.9 and 37.6 mAh/g at current densities of 0.05, 0.1, 0.2, 0.5, 1, 2, 5 and 10 A/g, respectively. Subsequently, the specific capacity was restored to 216.9 mAh/g when the current density was returned to 0.05 A/g (Fig. 4d and Fig. S8d in Supporting information). Notably, the rate capacities of $SnNb_2O_6$@CSN are obviously higher than that of $SnNb_2O_6$. Particularly, the rate performance of the free-standing $SnNb_2O_6$@CSN and other reported niobium-based oxides are compared in Fig. 4e, and the detailed data are summarized in Table S1 (Supporting information). The $SnNb_2O_6$@CSN material exhibits comparable and/or even better specific capacities than that of other niobium-based oxides [21,48–55]. The excellent electrochemical performance of $SnNb_2O_6$@CSN may be attributed to the following characteristics: (1) The 3D network conductive carbon skeleton (the carbon nanofiber has a large π-conjugated system, which can improve the electrical conductivity of the $SnNb_2O_6$@CSN) can shorten the transmission paths of ion/electron and improve the electrochemical transport kinetics. (2) 3D network structure provides abundant internal spaces to alleviate the volume expansion of $SnNb_2O_6$ upon cycling.

To better understand the differences in electrochemical kinetics and charge storage mechanism between $SnNb_2O_6$ and $SnNb_2O_6$@CSN, the CV experiments were performed between 0.01 V and 3.00 V. Fig. 4f shows the CV curves of $SnNb_2O_6$@CSN at different scanning rates. The anodic and cathodic peaks are basically stable when the scan rate increases to 1.2 mV/s. On contrast, the reduction/oxidation potentials of $SnNb_2O_6$ are slightly offset as the scanning rate increases (Fig. S12a in Supporting information). The current (i) and scanning rate (υ) obey the following formula [51,56]:

$$i = a\upsilon^b \tag{1}$$

where a and b are adjustable parameters. the b-value of 0.5 indicates a diffusion-controlled process, whereas b-value of 1 denotes the surface capacitance process. As shown in Fig. 4g, the b-values of the anodic and cathodic peaks for $SnNb_2O_6$@CSN electrode are 0.92 and 0.94, showing a dominated surface capacitive behavior. While the b values of the cathodic and anodic peaks for $SnNb_2O_6$ are 0.99 and 0.66, respectively, manifesting that the charge storage mechanism is co-controlled by capacitance and diffusion process (Fig. S12b in Supporting information). To quantitatively determine the contribution ratio of capacitance and diffusion-controlled in $SnNb_2O_6$@CSN, the following equation was used [24,57–59]:

$$i(\upsilon) = k_1\upsilon + k_2\upsilon^{1/2} \tag{2}$$

where i is the total current at a fixed voltage, and k_1 and k_2 are adjustable parameters. As shown in Fig. S12c (Supporting information), the CV curve was quantitatively divided into surface capacitance ($k_1\upsilon$) and diffusion-controlled process ($k_2\upsilon^{1/2}$). Based on this, Fig. 4h shows the contribution ratio of capacitance and diffusion-controlled of $SnNb_2O_6$@CSN at different scanning rates. It can be seen that 73% of the total capacity comes from the capacitance contribution at a scan rate of 0.1 mV/s, which gradually increases from 73% to 92% as the scan rate increases from 0.1 mV/s to 1.2 mV/s. While for $SnNb_2O_6$, the capacitance contribution is only 27% at 0.1 mV/s (Fig. S12d in Supporting information), which increases up to 59% when the scan rate increases to 1.2 mV/s (Fig. S12e in Supporting information). Obviously, the capacitance contribution of $SnNb_2O_6$@CSN is significantly higher than that of

$SnNb_2O_6$. The results indicate that the 3D carbon skeleton can improve the capacitive process of $SnNb_2O_6$@CSN, which is beneficial to accelerate the electron/ion transport kinetics.

Electrochemical impedance spectroscopy (EIS) measurement was carried out to further investigate the charge transfer kinetics of $SnNb_2O_6$ and $SnNb_2O_6$@CSN. As shown in Fig. 4i, the Nyquist plots of $SnNb_2O_6$ and $SnNb_2O_6$@CSN both consist of a semicircle in a high frequency region and a straight line in a low frequency region. The semicircle in the high frequency region corresponds to the charge transfer resistance (R_{ct}), which is associated with the electrode reaction, and the straight line at the low frequency region represents the Warburg impedance (Z_W), which is associated with the diffusion of sodium ions. Notably, the R_{ct} of $SnNb_2O_6$@CSN ($\sim$35.3 Ω) is significantly lower than that of $SnNb_2O_6$ ($\sim$53.2 Ω), which indicates that the 3D carbon skeleton can improve the conductivity of $SnNb_2O_6$@CSN material.

GITT measurements were used to investigated the electrochemical kinetics. The Na^+ diffusion coefficients (D_{Na^+}) were calculated according to the following formula:

$$D = \frac{4}{\pi\tau}\left(\frac{n_B V_M}{S}\right)^2\left(\frac{\Delta E_s}{\Delta E_t}\right)^2 \tag{3}$$

where τ stands for the relaxation time, s. n_B is the mole number of the active material, mol. V_M denotes the molar volume of the active material, cm^3/mol, S stands for the area of electrode, m^2/g. ΔE_s and ΔE_t can be obtained from the GITT curves. As shown in Fig. 4j, the D_{Na^+} values of the $SnNb_2O_6$@CSN are stable between 10^{-12} and 10^{-13} cm^2/s. While the D_{Na^+} values of $SnNb_2O_6$ (10^{-13}–10^{-14} cm^2/s) are obviously lower than that of $SnNb_2O_6$@CSN. This further confirms that the $SnNb_2O_6$@CSN with 3D carbon structure can effectively promote the Na^+ transmission.

Inspired by the excellent flexibility of the free-standing $SnNb_2O_6$@CSN electrode, the pouch cell was prepared with NaMNNb as cathode and the as-prepared $SnNb_2O_6$@CSN as anode. Figs. S13a and b (Supporting information) display the discharge-charge curves and the cycling performance of NaMNNb//$SnNb_2O_6$@CSN pouch cell at 0.05 A/g with a voltage range from 1.5 V to 3.9 V. In order to verify the practical application of the $SnNb_2O_6$@CSN electrode in SIBs, as shown in Figs. 4k–m and Movie S1 (Supporting information), the pouch cell can maintain light up LEDs at different bending angles (0°, 90°, 180°), which exhibits that the free-standing $SnNb_2O_6$@CSN electrode has great development potential in flexible electronic devices.

In summary, the free-standing $SnNb_2O_6$@CSN film with 3D carbon skeleton was successfully prepared as anode material by electrospinning and high temperature carbonization. The 3D carbon skeleton structure can shorten the transmission paths of ion/electron, improve the electrochemical reaction kinetics, as well as solve the issue of active materials detaching from the current collector during charging/discharging. Consequently, the as-prepared free-standing $SnNb_2O_6$@CSN exhibits excellent electrochemical performance (108.6 mAh/g at 10 A/g). The pouch cell can light up multiple LEDs at different blending angles. The remarkable electrochemical performance indicates that the free-standing $SnNb_2O_6$@CSN flexible electrode has great development potential in flexible electronic devices.

Declaration of competing interest

The authors declare that they have no known competing financial interests or personal relationships that could have appeared to influence the work reported in this paper.

Acknowledgments

This work was financially supported by the National Natural Science Foundation of China (Nos. 51774251, 22179077), the Natural Science Foundation in Shanghai (No. 21ZR1424200), the Shanghai Science and Technology Commission's "2020 Science and Technology In-novation Action Plan" (No. 20511104003), the Hebei Natural Science Foundation for Distinguished Young Scholars (No. B2017203313), and the Scientific Research Foundation for the Returned Overseas Chinese Scholars (No. CG2014003002).

Supplementary materials

Supplementary material associated with this article can be found, in the online version, at doi:10.1016/j.cclet.2022.107840.

References

[1] X. Wang, X. Yin, X. Feng, et al., Chem. Eng. J. 428 (2022) 130990.
[2] X. Feng, Y. Li, Q. Shi, et al., J. Energy Chem. 69 (2022) 442–449.
[3] L. Shen, Y. Li, S. Roy, et al., Chin. Chem. Lett. 32 (2021) 3570–3574.
[4] Y. Li, Y.F. Yuan, Y. Bai, et al., Adv. Energy Mater. 8 (2018) 1702781.
[5] Y. Liu, J. Li, Q. Shen, et al., eScience 2 (2022) 10–31.
[6] J.A.S. Oh, J. Sun, M. Goh, et al., Adv. Energy Mater. 11 (2021) 2101228.
[7] L. Zhao, Z. Qu, J. Energy Chem. 71 (2022) 108–128.
[8] Y.H. Xu, Y.J. Zhu, Y.H. Liu, et al., Adv. Energy Mater. 3 (2013) 128–133.
[9] Y. Wang, Y. Liu, Y. Liu, et al., J. Energy Chem. 54 (2021) 225–241.
[10] C.D. Zhao, J.Z. Guo, Z.Y. Gu, et al., Nano Res. 15 (2022) 925–932.
[11] X.P. Yin, Z.X. Lu, J. Wang, et al., Adv. Mater. 34 (2022) 2109282.
[12] X. Yin, Y. Zhao, X. Wang, et al., Small 18 (2022) e2105568.
[13] D.H. Youn, A. Heller, C.B. Mullins, Chem. Mater. 28 (2016) 1343–1347.
[14] A. Rudola, K. Saravanan, C.W. Mason, et al., J. Mater. Chem. A 1 (2013) 2653–2662.
[15] P. Wei, Y.X. Liu, Y.R. Su, et al., ACS Appl. Mater. Interfaces 11 (2019) 3116–3124.
[16] X. Wu, X. Lan, R. Hu, et al., Adv. Mater. 34 (2022) e2106895.
[17] L. Zhao, J.M. Zhao, Y.S. Hu, et al., Adv. Energy Mater. 2 (2012) 962–965.
[18] H. Park, H.B. Wu, T. Song, et al., Adv. Energy Mater. 5 (2015) 1401945.
[19] K. Tang, X.K. Mu, P.A. van Aken, et al., Adv. Energy Mater. 3 (2013) 49–53.
[20] A.M.L. Cruz, N.L. Alcaraz, A.F. Fuentes, et al., J. Power Sources 81 (1999) 255–258.
[21] M. Huang, J.X. Liu, P. Huang, et al., Rare Met. 40 (2021) 425–432.
[22] J. Yu, J. Deli, L. Di, et al., Catal. Sci. Technol. 7 (2017) 2308–2317.
[23] H. Wang, J. Yu, X. Zhan, et al., Appl. Surf. Sci. 528 (2020) 146938.
[24] T. Liu, X.M. Yin, X.P. Yin, et al., Chem. Asian J. 17 (2022) e202200288.
[25] L. David, R. Bhandavat, U. Barrera, et al., Nat. Commun. 7 (2016) 10998.
[26] S.T. Li, G. Liu, J. Liu, et al., J. Mater. Chem. A 17 (2016) 6426–6432.
[27] D. Zhang, H. Li, A. Riaz, et al., Energy Environ. Sci. 15 (2022) 185–195.
[28] T. Zhang, Z. Mao, X. Shi, et al., Energy Environ. Sci. 15 (2022) 158–168.
[29] S.S. Shi, Z. Li, L.Y. Shen, et al., Energy Storage Mater. 29 (2020) 78–83.
[30] M.K. Shobana, J. Alloy. Compd. 831 (2020) 154844–154861.
[31] S. Li, H. Guo, S. He, et al., Mater. Des. 214 (2022) 110406.
[32] B.H. Hou, Y.Y. Wang, Q.L. Ning, et al., Adv. Mater. 31 (2019) e1903125.
[33] S. Xiao, X. Li, W. Zhang, et al., ACS Nano 15 (2021) 13307–13318.
[34] X.X. Liu, C. Chen, Q. He, et al., Chem. Rec. 1 (2022) e202100294.
[35] Z. Liang, H. Tu, K. Zhang, et al., Chem. Eng. J. 437 (2022) 135421.
[36] Y. Jin, D. Jiang, D. Li, et al., ACS Sustain. Chem. Eng. 5 (2017) 9749–9757.
[37] B. Luo, Y. Hong, D. Li, et al., ACS Sustain. Chem. Eng. 6 (2018) 14332–14339.
[38] Z. Zhang, D. Jiang, D. Li, et al., Appl. Catal. B: Environ. 183 (2016) 113–123.
[39] J.S. Meng, Q. He, L.H. Xu, et al., Adv. Energy Mater. 9 (2019) 1802695.
[40] X. Liu, H. Wang, S. Zhang, et al., Electrochim. Acta 292 (2018) 759–768.
[41] J. Wang, G. Zhu, X. Liu, et al., J. Colloid Interface Sci. 533 (2019) 733–741.
[42] X. Zhou, L. Wan, Y. Guo, Adv. Mater. 25 (2013) 2152–2157.
[43] J. Lin, Y. Yuan, Q. Su, et al., Electrochim. Acta 292 (2018) 63–71.
[44] Z. Chen, W. Chen, H. Wang, et al., Nanoscale 12 (2020) 18673–18681.
[45] C. Wang, D. Higgins, F. Wang, et al., Nano Energy 9 (2014) 334–344.
[46] S. Lou, X. Cheng, L. Wang, et al., J. Power Sources 361 (2017) 80–86.
[47] L. Zhou, Z. Cao, W. Wahyudi, et al., ACS Energy Lett. 5 (2020) 766–776.
[48] F.F. Liu, X.L. Cheng, R. Xu, et al., Adv. Funct. Mater. 28 (2018) 1800394.
[49] L. She, Z. Yan, L. Kang, et al., ACS Omega 3 (2018) 15943–15951.
[50] L. Shen, Y. Wang, H. Lv, et al., Adv. Mater. 30 (2018) 1804378.
[51] Z. Tong, S. Liu, Y. Zhou, et al., Energy Storage Mater. 13 (2018) 223–232.
[52] B. Shang, Q. Peng, X. Jiao, et al., Ionics 25 (2019) 1679–1688.
[53] Y. Huang, X. Li, J. Luo, et al., ACS Appl. Mater. Interfaces 9 (2017) 8696–8703.
[54] Y. Wu, X. Fan, Y. Chen, et al., J. Mater. Chem. A 7 (2019) 20813–20823.
[55] K.Y. Xie, W.F. Wei, H.R. Yu, et al., RSC Adv. 6 (2016) 35746–35750.
[56] L. Wang, X. Bi, S. Yang, Adv. Mater. 28 (2016) 7672–7679.
[57] C. Lin, S. Deng, D.J. Kautz, et al., Small 13 (2017) 1702903.
[58] H. Zhang, X. Zhang, H. Li, et al., J. Colloid Interface Sci. 583 (2021) 652–660.
[59] Y. Yang, Y. Yue, L. Wang, et al., Int. J. Hydrog. Energy 45 (2020) 12583–12592.